Journal of Materials Chemistry A

PAPER

View Article Online
View Journal | View Issue

Cite this: J. Mater. Chem. A, 2019, 7, 11117

Ultra-high performance of Li/Na ion batteries using N/O dual dopant porous hollow carbon nanocapsules as an anode†

Linlin Wang, ‡*[a] Bo Lu, ‡[b] Saisai Wang,[ac] Wei Cheng,[d] Yufeng Zhao,[a] Jiujun Zhang*[a] and Xueliang Sun *[e]

Received 30th December 2018
Accepted 16th March 2019

DOI: 10.1039/c8ta12540f

rsc.li/materials-a

Carbon materials usually exhibit a low capacity, short cycle life and poor rate performance as anode materials for lithium ion batteries (LIBs) and sodium ion batteries (SIBs). It remains a great challenge to explore carbon materials for ultrafast lithium and sodium storage with both a high capacity and a long cycling stability. Herein, we report the fabrication of nitrogen (N)/oxygen (O) dual dopant hollow porous carbon nanocapsules that show a state-of-the-art electrochemical performance. If used as anodes for LIBs, at an ultrahigh current density of 30 A g^{-1}, the carbon nanocapsules can be cycled up to 11 000 cycles with a considerable capacity retention of ~310 mA h g^{-1}. For sodium storage, they also demonstrate an ultrastable cycling performance with a reversible capacity of ~150 mA h g^{-1} after 10 000 cycles at a high current density of 5 A g^{-1}. The outstanding electrochemical performance can be ascribed to the synergistic effects from heteroatom doping and the unique sealed porous hollow characteristics of the nanocapsules. Theoretical calculations suggest that the sealed capsule structure leads to a excellent mechanical stability, which can tolerate fast lithium/sodium intercalation and extraction at ultrahigh current densities.

Introduction

In recent years, urgent market demands for rechargeable batteries with high-energy and a high-power density have been prompted by the development of electric vehicles and hybrid electric vehicles.[1–3] Carbon materials are considered to be one of the most promising electrode materials for rechargeable batteries, particularly lithium-ion batteries (LIBs) and sodium-ion batteries (SIBs).[4–6] However, the intercalated graphite anode, the most commonly used commercial anode material for LIBs, suffers from a low theoretical capacity of only 372 mA h g^{-1} and a poor rate performance,[7] which is undoubtedly insufficient to satisfy future energy storage requirements. Furthermore, it cannot act as a host material for SIBs owing to its limited interlayer distance (~0.34 nm) and the larger radius of sodium ions (1.07 Å for Na^+ *vs.* 0.76 Å for Li^+).[8] Hence, it is critical to develop alternative carbon anode materials with an excellent rate performance and a high capacity with long cyclability to satisfy the increasing demand for high performance LIBs and SIBs.

To meet the requirements of a high-rate capability and long lifespan, unique nanostructures and heteroatom doping engineering represent two effective strategies to explore alternative carbon anode materials with high electrochemical performances. This is based on two facts, these are: the unique nanostructure (especially the porous/hollow structure) of the carbon materials[9–11] can improve the rate performance and cyclability for LIBs and SIBs which benefit from their kinetically favorable structures for ion and electron transport; and doping heteroatoms can significantly enhance the capacitive properties and the electric conductivity by tailoring the electronic and physicochemical characteristics of the carbon materials.[2,11–13] For example, nitrogen doping can generate extrinsic defects and increase the active sites of carbon anodes.[1,4–8,12,17,18] In addition, oxygen can also provide extra capacity by the redox reactions of the surface oxygen functional groups (such as –C=O + Li^+/Na^+ + e^- → –C–O–Li/Na).[11,15–18] Although various carbon materials, such as N-rich carbons[14] and oxygen-rich porous carbon[11] have been fabricated to improve the electrochemical performance, the rate capability and long-term cycling life practicality at

[a]Institute for Sustainable Energy, College of Science, Shanghai University, 99 Shangda Road, Shanghai 200444, P. R. China. E-mail: wlinlin@mail.ustc.edu.cn; jiujun.zhang@i.shu.edu.cn

[b]Shanghai Institute of Applied Mathematics and Mechanics, Shanghai University, 149 Yanchang Road, Shanghai 200072, China

[c]College of Chemistry and Chemical Engineering, Shanghai University of Engineering Science, 333 Longteng Road, Shanghai, 201620, P. R. China

[d]Department of Chemistry, The University of British Columbia, 2036 Main Mall, Vancouver, British Columbia, V6H1Z1, Canada

[e]Department of Mechanical and Materials Engineering, University of Western Ontario, 1151 Richmond St, London, Ontario, N6A 3K7, Canada. E-mail: xsun9@uwo.ca

† Electronic supplementary information (ESI) available. See DOI: 10.1039/c8ta12540f

‡ L. L. Wang and Bo Lu contributed equally.

a high current density still need to be improved for applications in high performance LIBs and SIBs. Therefore, there is still an urgent demand, as well as a significant challenge, to produce unique carbon nanostructures to simultaneously attain a high capacity and an ultralong life (and excellent cycling stability) at a high current density.

Based on the above considerations, in this work we combine the two strategies into one structure (*i.e.* N/O co-doped porous rod-like nanocapsules (N/O-CNCs) with a hollow feature). The strategy of a sacrificial template was applied for the controllable fabrication of the N/O-CNCs. The microstructure and composition of the N/O-CNCs were analyzed in detail. Theoretical calculations based on the analysis of the finite element method confirm the excellent mechanical stability of the sealed N/O-CNCs. By combining these advantages, the obtained N/O-CNCs deliver superb Li^+/Na^+ storage properties as expected. They can achieve a high reversible capacity of ~310 mA h g^{-1} after 11 000 cycles at an ultrahigh current density of 30 A g^{-1} for LIBs and ~150 mA h g^{-1} after 10 000 cycles for SIBs at a high current density of 5 A g^{-1}. The lithium storage performance and stability of the N/O-CNCs demonstrated the best values compared with other carbon materials reported to date (Table S1†). This ultralong cycle life with considerable capacity retention at the high current density of 5 A g^{-1} is also very competitive compared to previously reported carbon anode materials for SIBs (Table S2†). Remarkably, the N/O-CNCs also exhibit an excellent high rate performance for both LIBs and SIBs (especially for the rate capability and cycle life) (see Tables S1 and S2†).

Experimental

Material synthesis

The synthetic procedure used to prepare the N/O-CNCs consists of the deposition of polydopamine (PDA) on a Zn_2GeO_4 nanorod template, forming a Zn_2GeO_4 nanorod@PDA core–shell structure, followed by carbonization and chemical etching of the Zn_2GeO_4 nanorod template, resulting in a hollow N-doped porous carbon nanocapsule. An overall schematic illustration of the synthetic process is presented in Scheme 1. In a typical synthesis, 2.5 mmol $ZnCl_2$, 2.5 mmol GeO_2 and 0.5 mmol CTAB were dissolved into 15 mL of distilled water, forming an aqueous solution. The pH value was then adjusted to 8 by adding a 2 M NaOH solution at room temperature. The mixture was then transferred to a stainless-steel Teflon-lined autoclave and heated in an oven at 200 °C for 24 h. The resultant Zn_2GeO_4 nanorods were separated by centrifugation, washed, and dried. Afterwards, Zn_2GeO_4 nanorods (0.56 mmol) were dispersed in a mixed solution of ethanol (20 mL) and distilled water (15 mL). Subsequently, 0.79 mmol dopamine hydrochloride was added to the Zn_2GeO_4 nanorod suspension, followed by addition of tris(hydroxymethyl) aminomethane (Tris) and distilled water. The mixture was then continuously stirred and separated using centrifugation, and then washed and dried, forming the Zn_2GeO_4 nanorod@PDA core–shell structures (the Zn_2GeO_4@PDA were obtained using our previous method,[36] in which detailed characterization including the X-ray diffraction (XRD) patterns, scanning electron microscopy (SEM) and transmission electron microscopy (TEM) images were used to confirm the coating of PDA on the Zn_2GeO_4 nanorods). The as-formed material was then annealed at 600 °C for 4 h under a nitrogen atmosphere to produce the Zn_2GeO_4 nanorod@carbon shell. In the final step, the Zn_2GeO_4 nanorods@carbon shell was soaked in concentrated HCl for 2.5 days to remove the Zn_2GeO_4 (core). Finally, the resulting N/O-CNCs (denoted as N/O-CNCs-600) were separated using centrifugation, and washed thoroughly with water.

Characterization methods

The XRD patterns were measured on a Philips X'Pert X-ray diffractometer equipped with Cu Kα radiation ($\lambda = 1.5418$ Å). SEM images were acquired on a Hitachi SU-8010. TEM images were taken on a JEOL 2010F operating at 200 kV. The Raman spectroscopy measurement was carried out on a LABRAM-1B confocal laser micro-Raman spectrometer. N_2 sorption analysis was performed on a Micromeritics TriStar II 3020 nitrogen adsorption apparatus at 77 K. The specific surface area was calculated using the Brunauer–Emmett–Teller (BET) method. X-ray photoelectron spectra (XPS) were recorded on an ESCALab MKII X-ray photoelectron spectrometer.

Electrochemical measurements

The working electrode was prepared by mixing the active materials (80 wt%), acetylene black (Super-P) (10 wt%), and polyvinylidene fluoride (PVDF) (10 wt%) dissolved in *N*-methyl-2-pyrrolidinone. The above slurry was brush coated onto Cu foil with a coating thickness of 200 μm and dried at 110 °C for 24 h. The electrodes were then cut into disks and each sample was weighed three times using an electronic analytical balance (Sartorius, BT25S), in order to ensure the accuracy of the weight and material loading, and the obtained values were in a range of 0.4–0.5 mg cm^{-2}. Test cells (2016) were assembled in an argon-filled glove box using lithium metal as the anode, Celgard 2600 as the separator, and 1 M $LiPF_6$ (ethylene carbonate and dimethyl carbonate with a 1 : 1 volume ratio) as the electrolyte. The galvanostatic charge–discharge measurements were carried out on a Neware CT-3008 battery cycler (Guangdong, China) in the range of 0.01–3.0 V (*vs.* Li/Li^+). Cyclic voltammetry (CV) measurements were performed on an Autolab electrochemical workstation

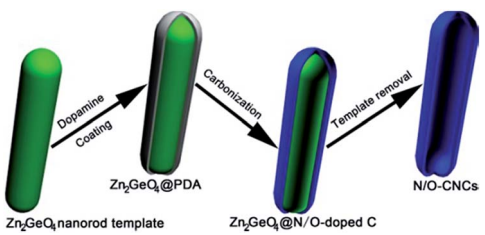

Scheme 1 Schematic illustration of the synthesis process for the N/O-CNCs.

(PGSTAT302N, Methrom, China). Electrochemical impedance spectroscopic (EIS) measurements of the cells were conducted on the same workstation with a sine wave of 5 mV over a frequency range of 100 kHz to 0.01 Hz.

Results and discussion

The morphology and microstructure of the as-synthesized N/O-CNCs-600 were investigated using SEM and TEM. As shown in Fig. 1a–d, the sample consists of a great number of uniform capsule-like nanorods with an average length of ~700 nm and an average diameter of ~100 nm, that is, an aspect ratio of ~7 : 1. The TEM image shown in Fig. 1d shows that there is a contrast difference between the central regions (light) and the edges including the ends (dark), indicating nanocapsules with an interesting two-end-sealed hollow interior. The higher magnification TEM image (Fig. 1e) further shows that the shell of the hollow nanocapsule has a thickness of ~15 nm, leaving a large cavity. A graphitic structure near the surface of the shell can be observed (Fig. 1f). The *d*-spacing between the adjacent graphene layers (d_{002}) is ~0.355 nm, which is larger than that of graphite (0.335 nm), suggesting a low graphitization degree for the N/O-CNCs-600.[37] The enlarged *d*-spacing of the (002) plane facilitates the intercalation/extraction of Li^+/Na^+, and the discontinuous graphene layers provide sufficient tunnels for ion diffusion, further improving the transport kinetics for Li^+/Na^+ storage.[33,37,38] The HAADF-STEM image and elemental maps (Fig. 1g) reveal that nitrogen, oxygen are homogeneously distributed around the entire carbon nanocapsule. EDS analysis (Fig. S1†) confirms the presence of N and O elements in the carbon nanocapsules. The N content in the N/O-CNCs-600 materials was calculated to be 6.6 wt%. More details regarding the as-prepared sample are summarized in Table S3 (ESI).† In our study, we tried to control the size of the N/O-CNCs-600 (Fig. S2†) by adjusting the template size of the Zn_2GeO_4 nanorods. It was found that a lower pH and a higher pH can result in a Zn_2GeO_4 template with a large size distribution and a poor dispersion, thus leading to synthesized N/O-CNCs with a large size distribution and a poor dispersion.

The porous characteristics of the carbon nanocapsule were confirmed using N_2 sorption analysis (Fig. 2a and Table S4†). The pore (>2 nm) size distribution curve calculated using the Barrett–Joyner–Halenda (BJH) method (inset, Fig. 2a) suggests the presence of mesopores and macropores. Sufficient and fast ionic diffusion can be achieved by the introduction of meso/macropores.[16] Also, as shown in Fig. 2b, a narrow distribution of 0.4–0.6 nm (Fig. 2b, plotted using the Horváth–Kawazoe (HK) method) confirms the existence of micropores, which is expected to be due to surface "cavity" defect sites. The BET surface area of the carbon nanocapsules is determined to be 471.6 $m^2 g^{-1}$. The Raman spectrum of the nanocapsules (Fig. 2c) presents a D-band at 1357 cm^{-1}, corresponding to disordered carbon and a G-band at 1593 cm^{-1}, corresponding to graphitic carbon.

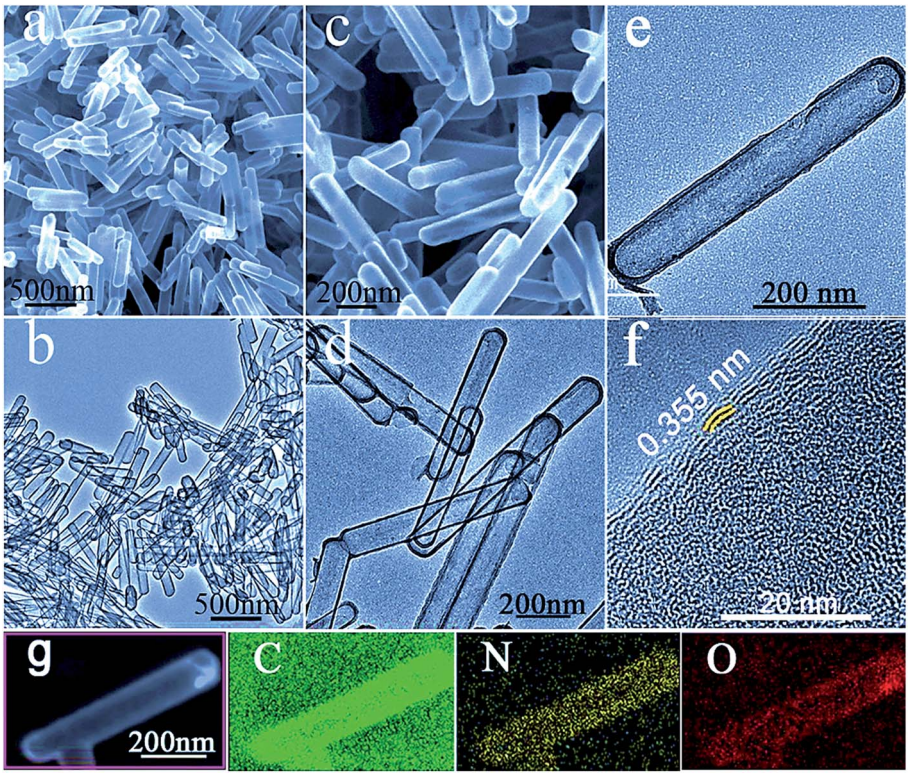

Fig. 1 (a) SEM image and (b) low-magnification TEM image of the N/O-CNCs-600. (c) TEM and (d) high resolution (HR)TEM images of a nanocapsule, respectively. (e–g) High angle annular dark field scanning transmission electron microscopy (HAADF-STEM) image and the corresponding energy-dispersive X-ray spectroscopy (EDS) elemental maps for C, N and O in the sample.

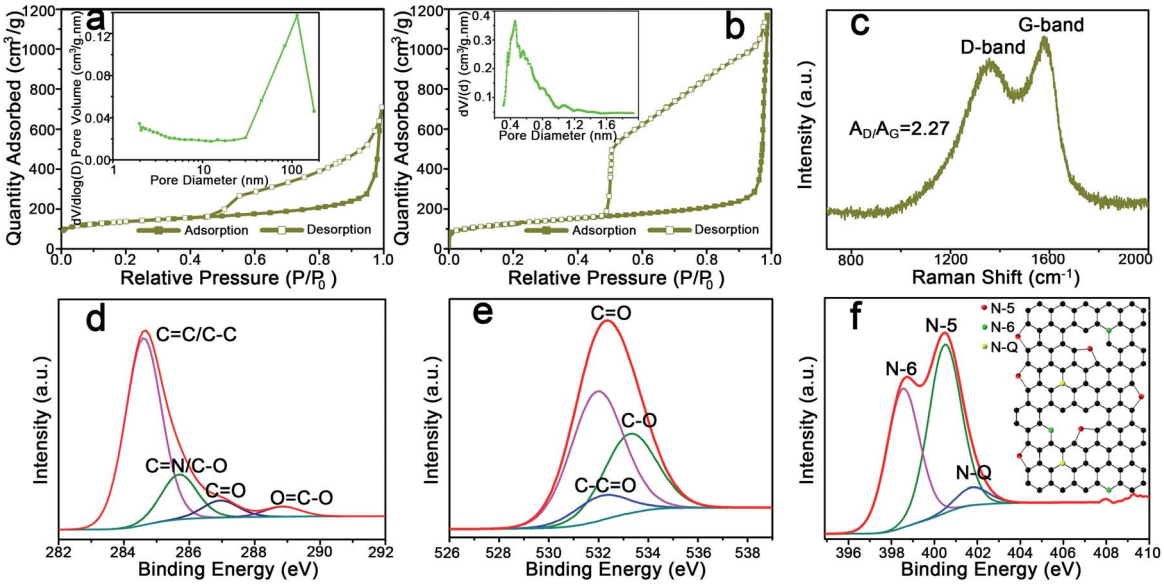

Fig. 2 (a and b) Microspore size distribution of the nitrogen adsorption–desorption isotherms, inset shows a micropore size distribution, calculated from adsorption isotherms using the HK method. (c) Raman spectrum. (d) C 1s, (e) O 1s and (f) N 1s XPS peaks.

The high intensity ratio of the D band to the G band (A_D/A_G) is 2.27. Such a high value implies the generation of numerous defects within the carbon nanocapsules owing to N-doping, which usually results in an enhancement in the capacitive properties.[20] In addition, a broad and weak second-order band at ~2700 cm^{-1} was also observed (Fig. S3†), in which the shapes of the 1D and 2D bands for this sample are characteristic of few-layered graphene.[1,39] XPS was used to examine the composition of the N/O-CNCs-600. Fig. 2d shows the C 1s peak, which can be resolved into four peaks corresponding to several kinds of carbon groups, these are C=C/C–C (~284.6 eV), C–O/C=N (~285.6 eV), C=O (~286.9 eV) and O–C=O (~289.0 eV), respectively.[40,41] The O 1s spectra of the sample (Fig. 2e) was deconvoluted into the three components of C=O (531.9 eV), O–C=O (532.0 eV), and C–O (533.2 eV). As shown in Fig. 2f, the N 1s spectrum can be fitted into three peaks, with maxima at 398.3, 400.3, and 401.4 eV, corresponding to pyridinic N (N-6), pyrrolic-N (N-5), and quaternary or graphitic (N-Q), respectively.[20,42] According to the fitting results of the N 1s spectra from the as-prepared N/O-CNCs, N-6 and N-5 are the dominant types (Table S3†). It should be noted that N-5 and N-6 dopants can reside at the edge or surface "hole" defect sites within the N/O-CNCs-600, instead of inside the graphitic carbon plane (see the inset in Fig. 2f).[19,24] Referring to previous studies,[1,19] the N atom substituents (N-6, N-5) at the periphery are the dominant N-containing functional groups in all of the PDA-derived N-doped carbon materials, and can serve as electrochemically active sites for enhancing the capacitive properties of the carbon materials for LIBs and SIBs.

Owing to the interesting microstructural characteristics of the as-synthesized N/O-CNCs-600, we first investigated its electrochemical properties as an anode in LIBs. Fig. 3a shows the first five CV scans of N/O-CNCs-600 from 0 to 3.0 V. The integral area of the first scan is much larger than that of the second scan owing to the decomposition of electrolyte, the formation of a solid electrolyte interface (SEI) film, and the reactions of lithium with the surface functional groups and the residual HCl.[21,22,43,44] After the first scan, the CV curves show a good overlap, implying the high reversibility and good cycling stability of the electrode. Fig. 3b shows the first discharge/charge profiles for the N-HRCNCs-600 electrode at 200 mA g^{-1}. The initial discharge and charge specific capacity are 2510 mA h g^{-1} and 1328 mA h g^{-1}, respectively. The irreversible capacity loss in the initial cycle can be ascribed to the reactions mentioned in the CV analysis. As shown in Fig. 3c, at 200 mA g^{-1} the electrode displays an excellent cyclic stability with a high capacity, maintaining a discharge capacity of 1100 mA h g^{-1} after 100 cycles. Fig. 3d shows the cycling performance of the N/O-CNCs-600 electrode at 10 A g^{-1}. The capacity slowly increases initially at several tens of cycles, and then gradually stabilizes, with a capacity retention of 420 mA h g^{-1} after 5000 cycles. At an extremely high current density of 30 A g^{-1} (~36 s full-charging time), the N/O-CNCs-600 electrode still remains at a steady reversible capacity of 310 mA h g^{-1}, even after 11 000 cycles (Fig. 3e). The significant increase in the capacity during cycling may result from an enhancement in the electronic chemical kinetics of the N/O-CNCs-600 after cycling, which was confirmed by EIS measurements of a fresh cell and an active cell after 11 000 cycles. The semicircle diameter of the N/O-CNCs-600 electrode after cycling is smaller than that of the N/O-CNCs-600 electrode before cycling (Fig. S4†), indicating that the interfacial charge-transfer resistance after cycling is reduced, which can be attributed to the activation of the electrode materials and to the easy and smooth electrolyte infiltration, facilitating rapid Li^+ transfer and storage.[32,42] Furthermore, our N/O-CNCs-600 electrode shows outstanding rate capabilities. As shown in Fig. 3f, the N/O-CNCs-600 electrode exhibits a high stable capacity of

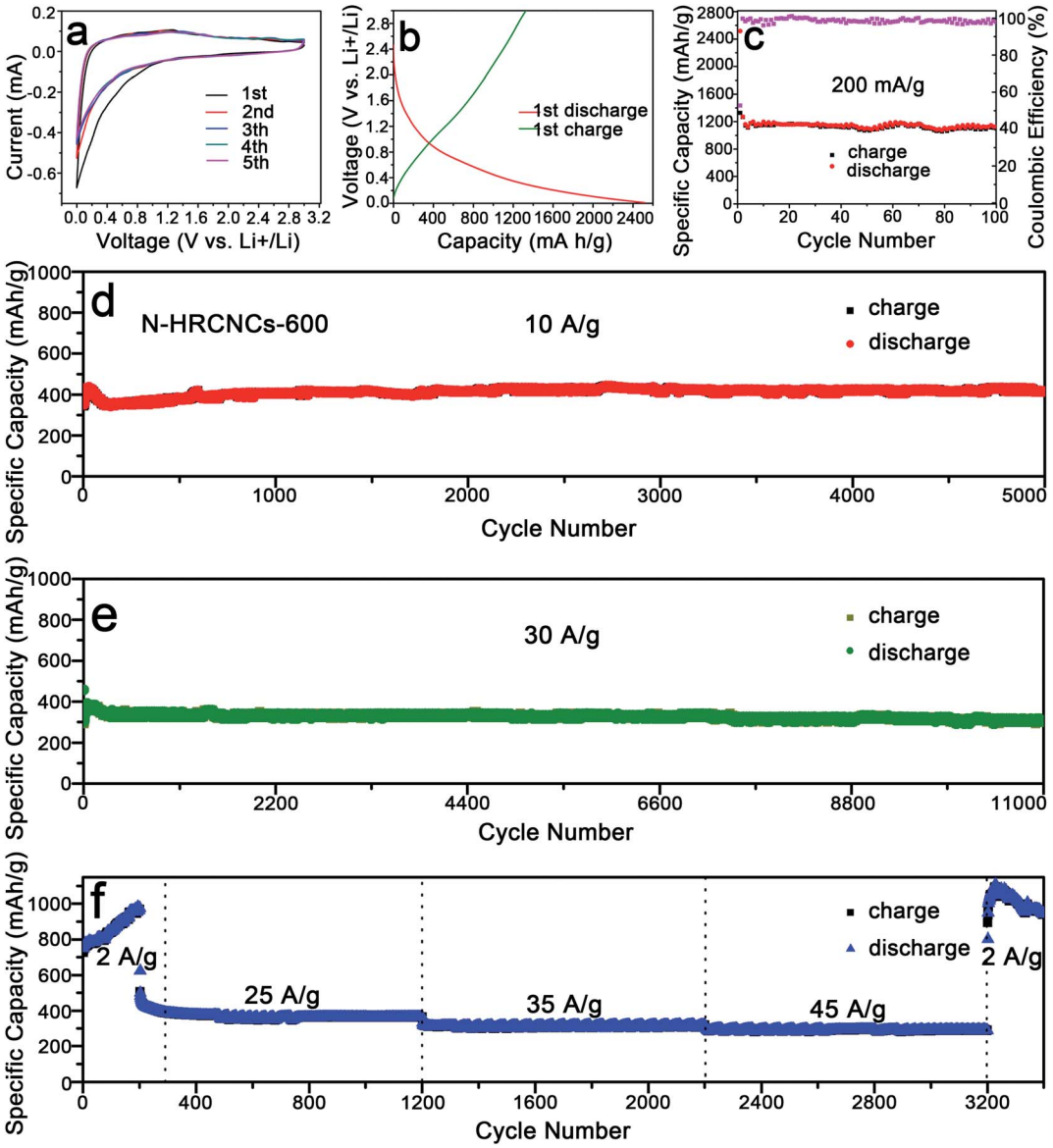

Fig. 3 Electrochemical performance of the N/O-CNCs-600 electrode for lithium ion battery (LIB) anodes: (a) CV curves of the initial 5 cycles at a scan rate of 0.1 mV s^{-1}. (b) Charge/discharge curve at 200 mA g^{-1}. Cycling performances at (c) 200 mA g^{-1}, (d) 10 A g^{-1} and (e) 30 A g^{-1}. (f) Rate capability at different current densities (the density was set at 0.3 A g^{-1} for the first cycle and from the third cycle).

980 mA h g^{-1} at 2 A g^{-1} after 200 cycles. As the current rate is increased stepwise to 25 A g^{-1} and 35 A g^{-1}, cycling for 1000 cycles at each rate, the capacity is reduced to 360 mA h g^{-1} and 320 mA h g^{-1}, respectively. Even at an ultrahigh current density of 45 A g^{-1}, a considerable capacity of 280 mA h g^{-1} can be still achieved after another 1000 cycles. After the rate is returned back to 2 A g^{-1}, a capacity of ~1000 mA h g^{-1} can be obtained. Fig. 4 compares the performance with previous reports (a comparison of the detailed parameters is also provided in Table S1†). It is obvious that the electrochemical performance of the N/O-CNCs-600 electrode, especially the extremely high rate and long cycle life metrics, are far superior to those reported for carbon materials (Table S1†).

Furthermore, the effect of the temperature on the electrochemical performance of the electrodes was investigated. We prepared the samples at different carbonization temperatures, for example, 500 and 700 °C (denoted as N/O-CNCs-500 and N/O-CNCs-700), with an N content of 6.8 wt% and 5.4 wt%, respectively (Table S5†), which have a similar morphology to those of N/O-CNCs-600 (Fig. S5†). More details about the composition and pore characteristics of the obtained samples are summarized in Tables S5 and S6,† respectively, which reveal they have a similar elemental composition and pore characteristics to N/O-CNCs-600 (Tables S3 and S4†). Their electrochemical performances are shown in Fig. 5a and b. Different from N/O-CNCs-700, an obvious capacity increase is observed for N/O-CNCs-500, especially at much higher current densities, and it gradually reaches almost the same capacity retention (410 mA h g^{-1} for 5000 cycles at 10 A g^{-1} and 300 mA h g^{-1} for 10 000 cycles at 30 A g^{-1}) as N/O-CNCs-700 (425 mA h g^{-1} for

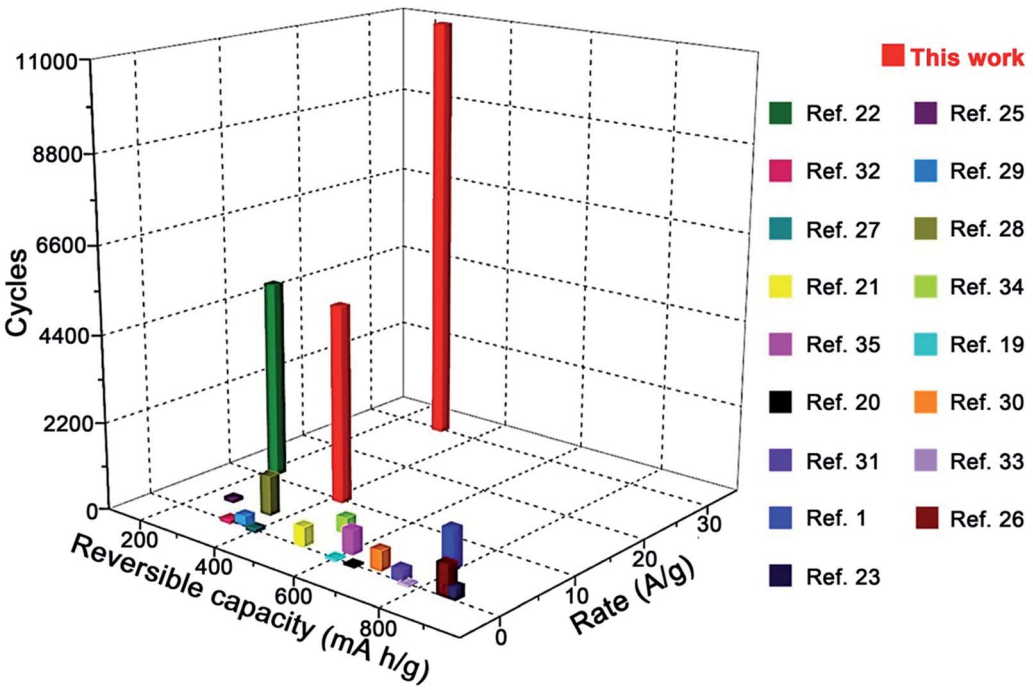

Fig. 4 A comparison between N/O-CNCs-600 and previous reports.

5000 cycles at 10 A g^{-1} and 290 mA h g^{-1} for 10 000 cycles at 30 A g^{-1}). For example, a continuous capacity increase is observed up to 2200 cycles and this then reaches a steady reversible capacity of 300 mA h g^{-1} after 11 000 cycles at 30 A g^{-1} (Fig. 5b). The difference could be attributed to the lower carbonization temperature (500 °C), leading to a slow activation of the N/O-CNCs-500 electrode. At low current (200 mA g^{-1}, for a time sufficient to induce activation), the electrode displays an excellent cyclic stability (Fig. S6†), supporting this point of view. There is no obvious difference between the electrochemical performance of N/O-CNCs-700 and N/O-CNCs-600. These results may be due to their similar elemental composition and pore characteristics relative to N/O-CNCs-600 (see Tables S3–S6†), which serves as the electrochemically active site for determining the reversible capacity of the N/O-CNCs. The superior electrochemical performances of

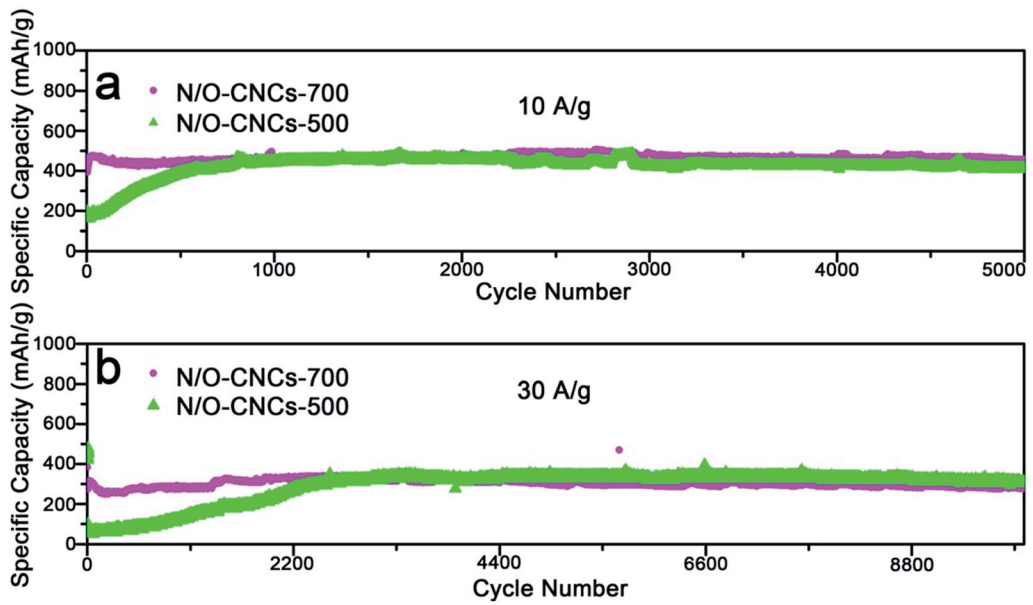

Fig. 5 (a and b) Electrochemical performances of the N/O-CNCs obtained at different carbonization temperatures (*i.e.*, 500 °C and 700 °C) at 10 and 30 A g^{-1}, respectively for LIB anodes (from the third cycle).

the N/O-CNCs electrodes for LIBs can be explained from the following perspectives: (i) N,O co-doping provides dual active binding sites for ion storage. On the one hand, oxygen can provide extra capacity owing to the redox reactions of the surface oxygen functional groups. On the other hand, doping induces defects in the carbon nanocapsules. In particular, a high proportion of doping of N-6 and N-5 among the total N dopants may play an important role in determining the reversible capacity.[1,45,46] By fitting peaks for the N 1s of these samples (*i.e.*, N/O-CNCs-500, N/O-CNCs-600 and N/O-CNCs-700), it is known that both N-6 and N-5 represent a high proportion of the doping among the total N dopants (Fig. 2f, S7, Tables S3 and S5†). For example, both N-6 and N-5 represent 94.5% in N/O-CNCs-600, which is higher than that in N-C-700 (~72.76%)[1] and the PMC (70.2%).[14] Such a high proportion of N-5 and N-6 gives rise to more edges or more surface defect sites from nanosized voids/cavities (see inset in Fig. 2f) except for small voids/cavities formed between the carbon sheets ("house-card" model).[47–49] These edges or surface defective sites can serve as more electrochemically active sites for storing the lithium species in a metallic cluster form, facilitating the transfer of Li^+ and electrons in the electrode, and enhancing the capacitive properties of the N/O-CNCs.[1,19,45,46,50] This lithium is stored in the small space, such as voids or cavities, in a metallic cluster form, this was also confirmed using low temperature Li-NMR.[51] However, the high reversible capacity of N/O-CNCs-600 (three times higher than that of graphite (372 mA h g^{-1})) is not only due to the contribution of lithium species held in the voids or cavities, but also to the lithium species intercalated into the interlayers. It is reasonable to assume that the lithium species are held in the cavities and intercalated into the interlayers at almost the same time, because no points of inflection are observed in the charge curves, as shown in Fig. 3b, this has also been proposed by Mabuchi *et al.*[45] Moreover, the lithium species in the form of lithium ions and Li_2 covalent molecules intercalated into the interlayers may also coexist, as the discharge capacities in the region between 0–0.9 V (see Fig. 3b) are much larger than that caused by a lithium-intercalated graphite intercalation compound.[48,52] In addition, the N-Q barely contributes to the capacity improvement, but the low N-Q content (5.5%) is beneficial for the structural stability of the N/O-CNCs, and thus helpful to the cycling stability.[1,17] (ii) The two-end sealed porous hollow characteristics of the carbon nanocapsules. A two-end sealed porous hollow carbon nanocapsule possesses an excellent mechanical stability, and this is beneficial for accommodating large volume changes and thus maintains a stable structure during the sustained charge–discharge process under ultrahigh current densities, resulting in ultralong cycling life with excellent stability. Here, these arguments can be supported by the theoretical calculations (please see ESI† for a detailed discussion). It was found that the peak stress for the sealed hollow capsule was much lower than that for the open-end one in terms of both lithium intercalation and extraction. This suggests that the sealed hollow capsule is a better structure for tolerating fast lithium intercalation/extraction (Fig. 6e). Experimentally, after 11 000 cycles, there was almost no morphological change observed for the N/O-CNCs electrodes (Fig. 6f), also indicating the structural robustness. In addition, in order to provide further evidence to support this view, we performed the following comparison experiments. First, we destroyed the sealed structure by complete grinding, then prepared the electrode. From the SEM

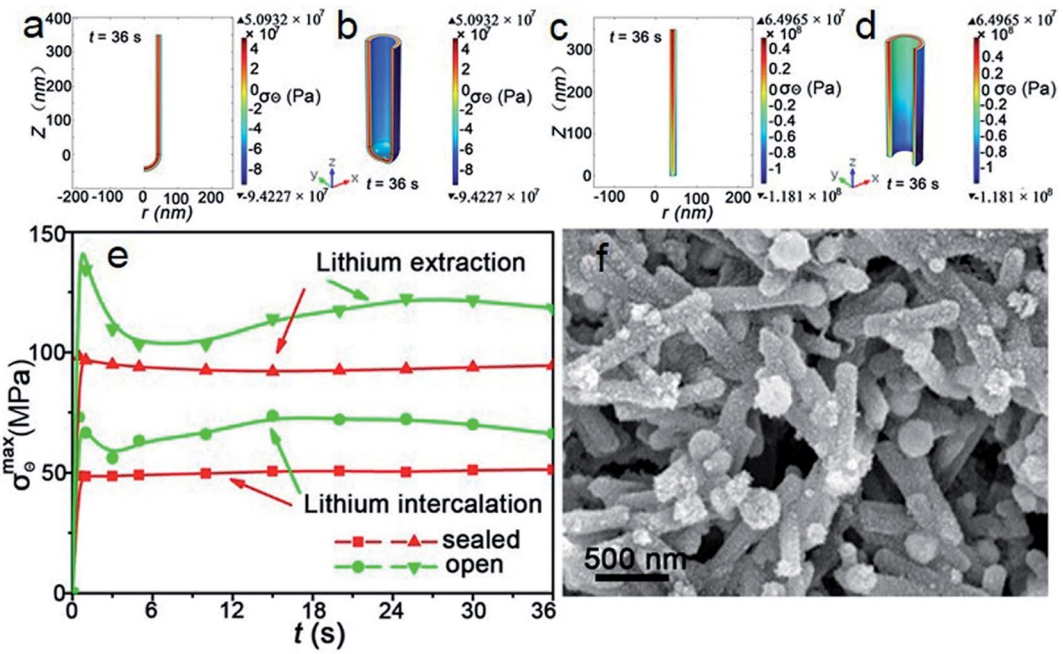

Fig. 6 The distribution of hoop stress in the sealed hollow capsule and in the open-end one, respectively: (a and c) axisymmetric cross-section; and (b and d) 3D rotation. (e) The maximum hoop stress with respect to intercalation/extraction time. (f) SEM image of the N/O-CNCs-600 electrode for LIB anodes after 11 000 charge/discharge cycles.

images (Fig. S8a†), it can be seen that after grinding, most of the sealed structures have been broken into open ones. The comparative cell only delivered a low capacity of ~60 mA h g^{-1} at an ultrahigh current density of 30 A g^{-1}, and as the current rate increases stepwise to 0.3 A g^{-1} and 2 A g^{-1}, the capacity decreases to ~500 mA h g^{-1} and 320 mA h g^{-1}, respectively. Furthermore, the capacity begins to decrease rapidly as the cycle number increases (Fig. S8b†). XPS analysis (Fig. S9†) reveals the composition of the ground sample is different from that of the unground sample, especially the O content, which can also confirm that the decreased capacities are attributed to the lost active binding sites during the grinding process. This suggests that the unique two-end sealed porous hollow nanocapsule structure might be critical for achieving the fast charge/discharge properties with an excellent cycling stability at extremely high current rates. Meanwhile, N/O-dual dopants can provide extra active binding sites for Li^+/Na^+ storage, which can enhance the energy-storage performance of the carbon electrodes. In addition, the porous characteristics of the carbon nanocapsules (Tables S4 and S6†) allow the electrolyte to flood into the pores, leading to a high electrolyte/electrode contact area and facile Li^+ transport in the electrolyte within the pores, giving further rise to the high rate capacity and cycling performances. As a result, the synergistic effects from the composition and the unique structure of the nanocapsules lead to the N/O-CNCs anode simultaneously achieving a high capacity, excellent rate capability, and ultralong cycling life.

As for application in SIBs, the electrodes were tested for both cycling and rate performance. Fig. 7a–c shows the cycling performance of N/O-CNCs-600 as an anode material for SIBs. A high Na^+ storage capacity and excellent cycling stability can be simultaneously achieved. It delivered a stable capacity of ~340 mA h g^{-1} for 300 cycles and ~230 mA h g^{-1} for 5000 cycles at 50 mA g^{-1} and 1 A g^{-1}, respectively. Even at a high current density of 5 A g^{-1}, a considerable capacity retention of ~150 mA h g^{-1} was still retained after 10 000 cycles. Except for the excellent cyclability, N/O-CNCs-600 also exhibits a good rate performance. When discharged at altering rates ranging from 0.05 A g^{-1} to 20 A g^{-1}, the electrode achieved a capacity of 330 mA h g^{-1} at 0.1 A g^{-1}, 270 mA h g^{-1} at 0.5 A g^{-1} and 105 mA h g^{-1} at 10 A g^{-1}. Even at 20 A g^{-1}, N/O-CNCs-600 still maintained a reversible capacity of 70 mA h g^{-1}. After the current returned to 200 mA g^{-1}, an enhanced storage capability, like that observed for the LIBs was obtained. This may also rely on the N/O dual dopants and the unique porous features of the nanocapsule. The sodium storage properties (especially for rate

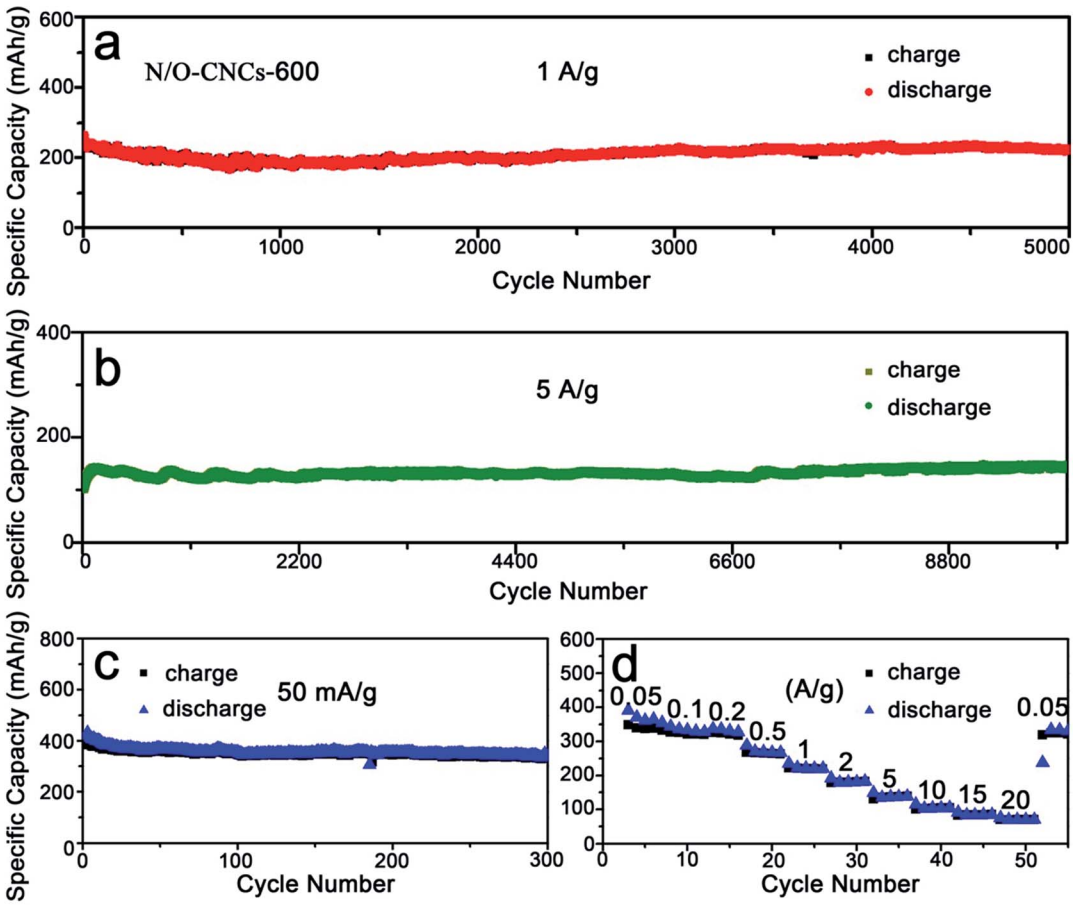

Fig. 7 Electrochemical performances of the N/O-CNCs-600 electrode for sodium ion battery (SIB) anodes: cycling performances at: (a) 1 A g^{-1}; (b) 5 A g^{-1}; and (c) 50 mA g^{-1}. (d) Rate capability at different current densities (the density was set at 0.05 A g^{-1} for the first cycle and from the second cycle).

capability and cycle life) of N/O-CNCs-600 are very competitive when compared with other reported carbon anode materials (Table S2†). In general, as Na^+ is larger than Li^+, most electrode materials for LIBs do not have a sufficiently large interstitial space within their crystallographic structure to host and transport Na^+.[16,53] In our case, the designed porous sealed capsule structure with N/O dual dopants provides a favorable path and active sites to satisfy both diffusion and the insertion/extraction of Li^+ and the larger Na^+.

Conclusions

In summary, we have successfully produced unique N/O co-doped porous carbon nanocapsules for energy storage. An excellent rate performance, high capacity and ultralong cycling life can be simultaneously achieved for storage of both Li^+/Na^+. The outstanding electrochemical performances of the N/O-CNCs can be ascribed to: (1) N/O-dual dopants providing extra active binding sites for Li^+/Na^+ storage, which enhance the energy-storage performance of the carbon electrodes; and (2) the unique sealed hollow capsule structure has an excellent mechanical stability which can tolerate fast lithium intercalation and extraction at ultrahigh current densities, which is supported by the theoretical calculations. Furthermore, the porous characteristics of the carbon nanocapsules allows the electrolyte to flood into the pores, leading to a high electrolyte/electrode contact area and facile Li^+/Na^+ transport in the electrolyte within the pores, giving further rise to the high rate capacity and cycling performances. Our work could provide new clues for the development of ultrafast carbon anodes with a high performance. Moreover, the synthetic strategy developed here could be extended for fabrication of various new hollow/porous carbonaceous nanomaterials for the increasing demands of high power density by electronic devices.

Conflicts of interest

There are no conflicts to declare.

Acknowledgements

This work was supported by the National Natural Science Foundation of China (No. 21601122, 51774253) and sponsored by Shanghai Sailing Program (No. 14YF1409700). We thank Prof. Qianwang Chen and Prof. Kaibin Tang at the University of Science and Technology of China for discussion about the mechanism. We thank Prof. Yanwei Ding at the University of Science and Technology of China for discussion about the pore size distribution. We thank Prof. Junqing Hu at Donghua University and Prof. Gen Chen at Central South University for discussion about the work.

Notes and references

1 F. Zheng, Y. Yang and Q. Chen, *Nat. Commun.*, 2014, **5**, 1.
2 J. Lu, Z. W. Chen, F. Pan, Y. Cui and K. Amine, *Electrochem. Energy Rev.*, 2018, **1**, 35.
3 Y. Fang, L. Xiao, Z. Chen, X. Ai, Y. Cao and H. Yang, *Electrochem. Energy Rev.*, 2018, **1**, 294.
4 W. H. Shin, H. M. Jeong, B. G. Kim, J. K. Kang and J. W. Choi, *Nano Lett.*, 2012, **12**, 2283.
5 S. Komaba, W. Murata, T. Ishikawa, N. Yabuuchi, T. Ozeki, T. Nakayama, A. Ogata, K. Gotoh and K. Fujiwara, *Adv. Funct. Mater.*, 2011, **21**, 3859.
6 H. S. Hou, C. E. Banks, M. J. Jing, Y. Zhang and X. B. Ji, *Adv. Mater.*, 2015, **27**, 7861.
7 C. C. Ma, X. H. Shao and D. P. Cao, *J. Mater. Chem.*, 2012, **22**, 8911.
8 A. P. Vijaya Kumar Saroja, M. Muruganathan, K. Muthusamy, H. Mizuta and R. Sundara, *Nano Lett.*, 2018, **18**, 5688.
9 S. B. Yang, X. L. Feng, L. J. Zhi, Q. A. Cao, J. Maier and K. Mullen, *Adv. Mater.*, 2010, **22**, 838.
10 Z. Y. Lyu, L. J. Yang, D. Xu, J. Zhao, H. W. Lai, Y. F. Jiang, Q. Wu, Y. Li, X. Z. Wang and Z. Hu, *Nano Res.*, 2015, **8**, 3535.
11 Y. Zhang, Y. Meng, Y. Wang, L. Chen, Y. Guo and D. Xiao, *ChemElectroChem*, 2017, **4**, 500.
12 H. S. Hou, L. D. Shao, Y. Zhang, G. Q. Zou, J. Chen and X. B. Ji, *Adv. Sci.*, 2017, **4**, 1600243.
13 G. Q. Zou, H. S. Hou, C. W. Foster, C. E. Banks, T. X. Guo, Y. L. Jiang, Y. Zhang and X. B. Ji, *Adv. Sci.*, 2018, **5**, 1800241.
14 Z. Li, Z. Xu, X. Tan, H. Wang, C. M. B. Holt, T. Stephenson, B. C. Olsen and D. Mitlin, *Energy Environ. Sci.*, 2013, **6**, 871.
15 H. R. Byon, B. M. Gallant, S. W. Lee and Y. Shao-Horn, *Adv. Funct. Mater.*, 2013, **23**, 1037.
16 J. He, N. Wang, Z. Cui, H. Du, L. Fu, C. Huang, Z. Yang, X. Shen, Y. Yi, Z. Tu and Y. Li, *Nat. Commun.*, 2017, **8**, 1172.
17 L. Fan and B. A. Lu, *Small*, 2016, **12**, 2783.
18 S. W. Lee, N. Yabuuchi, B. M. Gallant, S. Chen, B. S. Kim, P. T. Hammond and Y. Shao-Horn, *Nat. Nanotechnol.*, 2010, **5**, 531.
19 X. Wang, Q. H. Weng, X. Z. Liu, X. B. Wang, D. M. Tang, W. Tian, C. Zhang, W. Yi, D. Q. Liu, Y. Bando and D. Golberg, *Nano Lett.*, 2014, **14**, 1164.
20 X. C. Liu, S. M. Li, J. Mei, W. M. Lau, R. Mi, Y. C. Li, H. Liu and L. M. Liu, *J. Mater. Chem. A*, 2014, **2**, 14429.
21 K. L. Zhang, X. N. Li, J. W. Liang, Y. C. Zhu, L. Hu, Q. S. Cheng, C. Guo, N. Lin and Y. T. Qian, *Electrochim. Acta*, 2015, **155**, 174.
22 X. Liu, D. Chao, Y. Li, J. Hao, X. Liu, J. Zhao, J. Lin, H. Jin Fan and Z. Xiang Shen, *Nano Energy*, 2015, **17**, 43.
23 X. N. Li, X. Zhu, Y. C. Zhu, Z. Q. Yuan, L. L. Si and Y. T. Qian, *Carbon*, 2014, **69**, 515.
24 Z. S. Wu, W. Ren, L. Xu, F. Li and H. M. Cheng, *ACS Nano*, 2011, **5**, 5463.
25 Y. S. Hu, P. Adelhelm, B. M. Smarsly, S. Hore, M. Antonietti and J. Maier, *Adv. Funct. Mater.*, 2007, **17**, 1873.
26 C. Shen, C. C. Zhao, F. X. Xin, C. Cao and W. Q. Han, *Electrochim. Acta*, 2015, **180**, 852.
27 X. F. Li, J. Liu, Y. Zhang, Y. L. Li, H. Liu, X. B. Meng, J. L. Yang, D. S. Geng, D. N. Wang, R. Y. Li and X. L. Sun, *J. Power Sources*, 2012, **197**, 238.
28 G. H. Wu, R. Y. Li, Z. J. Li, J. K. Liu, Z. G. Gu and G. L. Wang, *Electrochim. Acta*, 2015, **171**, 156.

29 W. Wang, I. Ruiz, S. Guo, Z. Favors, H. H. Bay, M. Ozkan and C. S. Ozkan, *Nano Energy*, 2014, **3**, 113.
30 X. Liu, Y. Wu, Z. Yang, F. Pan, X. Zhong, J. Wang, L. Gu and Y. Yu, *J. Power Sources*, 2015, **293**, 799.
31 T. Mei, L. Zhang, X. B. Wang and Y. T. Qian, *J. Mater. Chem. A*, 2014, **2**, 11974.
32 Y. H. Hu, X. F. Li, J. J. Wang, R. Y. Li and X. L. Sun, *J. Power Sources*, 2013, **237**, 41.
33 F. D. Han, Y. J. Bai, R. Liu, B. Yao, Y. X. Qi, N. Lun and J. X. Zhang, *Adv. Energy Mater.*, 2011, **1**, 798.
34 Z. Q. Xie, Z. Y. He, X. H. Feng, W. W. Xu, X. D. Cui, J. H. Zhang, C. Yan, M. A. Carreon, Z. Liu and Y. Wang, *ACS Appl. Mater. Interfaces*, 2016, **8**, 10324.
35 S. Zhu, J. J. Li, L. Y. Ma, L. C. Guo, Q. Y. Li, C. N. He, E. Z. Liu, F. He, C. S. Shi and N. Q. Zhao, *ACS Appl. Mater. Interfaces*, 2016, **8**, 11720.
36 X. Z. Zhang, L. L. Wang, Y. Zou, X. Peng, M. Zhang, S. A. Gao, J. L. Xu, K. B. Tang and D. L. Zhao, *Mater. Lett.*, 2016, **166**, 243.
37 Y. Liu, X. D. Yan, Y. H. Yu and X. P. Yang, *J. Mater. Chem. A*, 2015, **3**, 20880.
38 J. Sun, H. M. Liu, X. Chen, D. G. Evans, W. S. Yang and X. Duan, *Adv. Mater.*, 2013, **25**, 1125.
39 A. C. Ferrari and D. M. Basko, *Nat. Nanotechnol.*, 2013, **8**, 235.
40 S. K. Xian, F. Xu, Z. X. Zhao, Y. W. Li, Z. Li, Q. B. Xia, J. Xiao and H. H. Wang, *AIChE J.*, 2016, **62**, 3730.
41 X. J. Wang, Y. Wu, X. Zhou, J. Xiao, Q. B. Xia, H. H. Wang and Z. Li, *Chem. Eng. Sci.*, 2016, **155**, 338.
42 A. L. M. Reddy, A. Srivastava, S. R. Gowda, H. Gullapalli, M. Dubey and P. M. Ajayan, *ACS Nano*, 2010, **4**, 6337.
43 Z. Yang, H. Q. Wu and B. Simard, *Electrochem. Commun.*, 2002, **4**, 574.
44 C. Hu, L. Wang, Y. Zhao, M. Ye, Q. Chen, Z. Feng and L. Qu, *Nanoscale*, 2014, **6**, 8002.
45 A. Mabuchi, K. Tokumitsu, H. Fujimoto and T. Kasuh, *J. Electrochem. Soc.*, 1995, **142**, 1041.
46 Y. P. Wu, S. B. Fang and Y. Y. Jiang, *Solid State Ionics*, 1999, **120**, 117.
47 J. S. Xue and J. R. Dahn, *J. Electrochem. Soc.*, 1995, **142**, 3668.
48 J. R. Dahn, T. Zheng, Y. H. Liu and J. S. Xue, *Science*, 1995, **270**, 590.
49 M. Nagao, C. Pitteloud, T. Kamiyama, T. Otomo, K. Itoh, T. Fukunaga, K. Tatsumi and R. Kanno, *J. Electrochem. Soc.*, 2006, **153**, A914.
50 H. S. Oktaviano, K. Yamada and K. Waki, *J. Mater. Chem.*, 2012, **22**, 25167.
51 K. Tatsumi, J. Conard, M. Nakahara, S. Menu, P. Lauginie, Y. Sawada and Z. Ogumi, *J. Power Sources*, 1999, **81**, 397–400.
52 K. Sato, M. Noguchi, A. Demachi, N. Oki and M. Endo, *Science*, 1994, **264**, 556.
53 Y. Cao, L. Xiao, M. L. Sushko, W. Wang, B. Schwenzer, J. Xiao, Z. Nie, L. V. Saraf, Z. Yang and J. Liu, *Nano Lett.*, 2012, **12**, 3783.